https://doi.org/10.5194/egusphere-2026-2980
Preprint. Discussion started: 13 July 2026

Droplet sedimentation regulates liquid water in marine advection fog: Large-eddy simulations with interactive sectional microphysics

Sijie Li[1,2★], Wei Dai[3★], Jing-Wu Liu[1,2*], Liu Yang[4], Shanhong Gao[1,2]

[1]State Key Laboratory of Physical Oceanography, Ocean University of China, Qingdao, China

[2]College of Oceanic and Atmospheric Sciences, Ocean University of China, Qingdao, China

[3]Qingdao Eco-environment Monitoring Center of Shandong Province, Qingdao, China

[4]College of Aviation Meteorology, Civil Aviation Flight University of China, Chengdu, China

★These authors contributed equally to this work.

*Corresponding author: Jing-Wu Liu, Ocean University of China, 238 Songling Road, Qingdao, 266100, P. R. China

Email: liujingwu@126.com; liujingwu@ouc.edu.cn

https://doi.org/10.5194/egusphere-2026-2980
Preprint. Discussion started: 13 July 2026

Abstract

Marine advection fog strongly affects visibility and maritime operations, yet numerical models frequently overestimate its liquid water content. Although fog-top radiative cooling is known to promote condensation, how size-dependent gravitational droplet sedimentation redistributes and removes the resulting liquid water remains poorly quantified. Here, we use the University of California, Los Angeles Large-Eddy Simulation model coupled with the sectional aerosol–cloud microphysics module from a Lagrangian perspective to quantify this process during a typical advection-fog event over the northwestern Pacific. Longwave radiative cooling near the fog top promotes condensational growth and the formation of large droplets, generating intermittent sedimentation signals that propagate downward through the fog layer. Lead–lag correlations show that sedimentation initiated near the fog top reaches the fog base after approximately 1 h. The liquid water path budget identifies fog-top radiative cooling as the dominant source (about 30 g m^{-2} h^{-1}) and gravitational sedimentation as the largest microphysical sink (approximately 20 g m^{-2} h^{-1}), offsetting nearly two-thirds of the radiatively driven production. Droplets with radii larger than 10 μm dominate the sedimentation flux. Sensitivity experiments confirm the robustness of this mechanism: removing sedimentation causes excessive liquid-water accumulation and substantially deepens the fog layer, while suppressed collision–coalescence or enhanced aerosol loading weakens sedimentation by limiting large-droplet formation. These results identify droplet sedimentation as a vertically coupled control on liquid-water redistribution and fog-layer evolution, implying that marine-fog parameterizations need to represent sedimentation and large-droplet microphysics explicitly.

https://doi.org/10.5194/egusphere-2026-2980
Preprint. Discussion started: 13 July 2026

1. Introduction

Sea fog is an important marine weather hazard because the associated low visibility severely limits maritime transportation and poses substantial risks to navigation safety. In some coastal regions, the economic losses caused by sea fog have been reported to be comparable to those associated with typhoons (Gultepe et al., 2007). However, the accurate prediction of sea fog remains a longstanding challenge for numerical weather prediction (NWP) models, partly because their coarse spatial resolution cannot adequately represent the tight coupling among turbulence, microphysical processes, and radiative effects within the shallow fog layer (Fernando et al., 2025; Gultepe et al., 2017; Koračin et al., 2014), which is typically only a few hundred meters deep.

A major deficiency of current NWP models is their tendency to produce excessively dense fog, as reflected by an overestimation of fog liquid water content (LWC). Observations show that near-surface LWC is typically below 0.2 g m^{-3} (Fernandez et al., 2025; Gultepe et al., 2009; Isaac et al., 2020; Wang et al., 2020), whereas simulated values often exceed 0.4 g m^{-3} (Chen et al., 2020; Taylor et al., 2021). Chen et al. (2020), for example, found that across multiple marine fog events, five planetary boundary layer schemes produced LWC values two to three times larger than observed. Because visibility in NWP models is largely diagnosed from LWC, this bias directly leads to underestimated visibility and, consequently, high false-alarm rates in sea fog forecasts. For instance, Xiang et al. (2025) reported that the 24 h false-alarm rate of sea fog forecasts from the Weather Research and Forecasting (WRF) model reached 85 %, whereas machine-learning-based post-processing reduced this rate by about 10 %.

To alleviate the overestimation of fog LWC in NWP simulations, Taylor et al. (2021) introduced a downward LWC flux at the lowest model level to reduce excessive LWC. This parameterization was based on constant-flux-layer theory and extended to account for both gravitational settling and turbulence-induced deposition. It can be regarded as a physically motivated revision of the interception–sedimentation treatment proposed by Katata et al., (2011). More generally, fog droplet removal involves several distinct processes, including surface interception, turbulent deposition, and gravitational settling. In the following discussion, fog droplet sedimentation refers specifically to gravitational sedimentation unless otherwise noted.

Observed fog droplet size distributions are often broad and sometimes bimodal. Issac et al. (2020), for example, reported two peaks at droplet diameters of approximately 6 and 24 μm. In sea fog, droplet number concentrations are typically on the order of 100 cm^{-3}. If all droplets are assumed to have a diameter $d = 6$ μm, the corresponding sedimentation flux

https://doi.org/10.5194/egusphere-2026-2980
Preprint. Discussion started: 13 July 2026

is only about 0.045 g m^{-2} h^{-1}. Under Stokes' law, terminal fall speed scales as d^2, the sedimentation flux therefore scales approximately as d^5. Consequently, a single droplet with d = 24 µm contributes roughly an order of magnitude more to the sedimentation flux than the combined contribution of 100 droplets with d = 6 µm. Considering that the liquid water path (LWP) of sea fog is typically less than 1 kg m^{-2}, gravitational sedimentation may constitute a substantial liquid-water sink during multi-day fog events (Fig. 1).

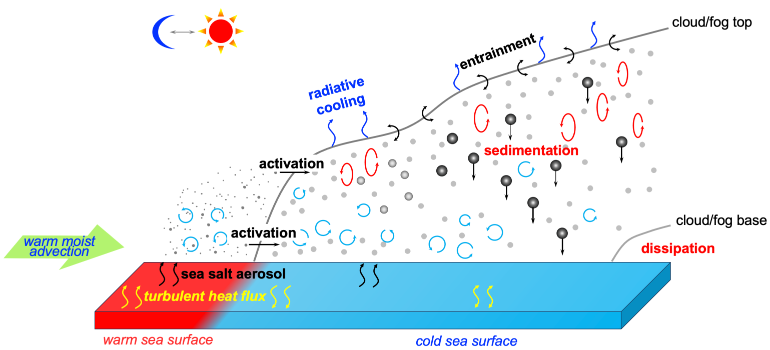

Figure 1. Schematic illustration of advection fog evolution. Warm, moist air advects from the warm flank to the cold flank of an SST front, where surface cooling and enhanced downward turbulent heat flux favor droplet activation and fog formation. As the fog layer deepens, radiative cooling at the fog top enhances turbulence and entrainment of warm, dry air from aloft, while gravitational settling and surface deposition progressively remove liquid water. These processes together regulate the development, vertical structure, and eventual dissipation of the fog layer.

However, most numerical models have limited capability to represent the influence of large droplets on sea fog evolution. In one-moment microphysics schemes, droplet number concentration is usually prescribed or fixed, making it difficult to estimate sedimentation fluxes realistically (e.g., Lin et al., 1983). Two-moment schemes, although prognosing both mass and number concentrations, still rely on an assumed functional form of the droplet size distribution and therefore have limited ability to capture the disproportionate contribution of relatively large droplets. As a result, the effects of gravitational sedimentation may be substantially underestimated in current fog simulations. To our knowledge, Barve et al. (2025) presented the first successful reproduction of the observed bimodal droplet spectrum in marine fog using LES coupled with a Lagrangian cloud model based on the superdroplet method. However, the specific role of large-droplet sedimentation in sea fog evolution was not explicitly examined.

Recent studies further imply that gravitational sedimentation is not confined to the fog base. For example, super-droplet simulations showed that the settling of relatively large droplets near cloud top can substantially modify the vertical distribution of liquid water and the liquid water path (Yin et al., 2024), while high-resolution lidar observations

https://doi.org/10.5194/egusphere-2026-2980
Preprint. Discussion started: 13 July 2026

revealed pronounced vertical stratification associated with size-dependent droplet settling near cloud top (Yang et al., 2025). Single-column modeling further indicates that under lower aerosol concentrations, larger droplets settle faster, promoting earlier cloud-base lowering, while simultaneously accelerating liquid-water loss to the surface and suppressing fog water content. Nevertheless, the role of gravitational sedimentation in advection fog—one of the most common fog types over the open ocean—remains poorly understood.

Advection fog typically forms when warm, moist air is advected over a colder ocean surface and cooled to saturation, thereby triggering condensation and fog formation (Fig. 1). During boreal summer, this type of fog is particularly common over the cold flanks of the Kuroshio Extension and Gulf Stream fronts in the North Pacific and North Atlantic, respectively (Koračin et al., 2014). In these regions, warm and humid airflow along the northwestern periphery of the subtropical high often crosses sharp sea-surface temperature (SST) fronts, creating favorable conditions for frequent fog occurrence. Along the Kuril Islands, for example, sea-fog frequency exceeds 70% in July and August (Tokinaga and Xie, 2009).

In our previous studies, we examined a typical advection-fog event over the northwestern Pacific using UCLALES (the University of California, Los Angeles Large-Eddy Simulation model), with the analysis framed from a Lagrangian perspective. The results show that once warm, moist air crosses the Kuroshio Extension SST front and fog forms, longwave radiative cooling (LRC) becomes the dominant cooling mechanism within about 2 h (Yang et al., 2024). This radiative cooling promotes water-vapor condensation and liquid-water accumulation near the fog top, which in turn strengthens LRC and establishes a positive feedback that enhances fog development and helps sustain its subsequent evolution. At a later stage, however, LRC-induced turbulence near the fog top enhances the entrainment of warm, dry free-tropospheric air into the boundary layer, reducing near-surface humidity and ultimately lifting the cloud base off the sea surface, thereby transforming the fog into stratus (Yang et al., 2021). Nevertheless, UCLALES employs a two-moment warm-rain bulk microphysics scheme, in which cloud microphysical processes are highly simplified (Seifert and Beheng, 2001; Stevens et al., 2005). As a result, the simulated near-surface LWC exceeds 1 g m^{-3}, indicating a substantial overestimation of fog water content (Yang et al., 2021, 2024).

The present study extends the large-eddy simulations (LESs) of Yang et al. (2021, 2024) to investigate the effects of droplet sedimentation on advection fog evolution using UCLALES–SALSA, which couples UCLALES with the sectional aerosol–cloud

https://doi.org/10.5194/egusphere-2026-2980
Preprint. Discussion started: 13 July 2026

microphysics module SALSA (Kokkola et al., 2008; Tonttila et al., 2017). In contrast to bulk microphysics schemes, SALSA uses a spectral bin framework to predict the number and mass mixing ratios of aerosol particles, cloud droplets, and precipitation particles. This framework explicitly resolves key microphysical processes, including aerosol activation, condensational growth, evaporation, collision–coalescence, and sedimentation, and is therefore better suited for examining the role of droplet sedimentation in advection fog.

This study aims to clarify how gravitational droplet sedimentation regulates the evolution of marine advection fog by explicitly resolving droplet-size-dependent microphysical processes. This work provides a process-level assessment of sedimentation as a vertically coupled pathway that connects fog-top liquid-water production with near-surface liquid-water removal. The results are expected to improve physical understanding of liquid-water regulation in marine fog and to provide guidance for representing droplet sedimentation and large-droplet microphysics in fog parameterizations.

The rest of the paper is organized as follows. Section 2 describes the observational datasets, model configuration, and experimental design. Section 3 presents the synoptic evolution and satellite-observed microphysical characteristics of the sea-fog event. Section 4 examines the simulated fog evolution, droplet sedimentation processes, and liquid-water budget. Section 5 discusses the sensitivity experiments. Finally, Section 6 summarizes the main conclusions and discusses their implications.

2. Data and methods

2.1 ICOADS, MODIS and reanalysis

We use the International Comprehensive Ocean–Atmosphere Data Set (ICOADS; Worley et al., 2005) to examine the occurrence of sea fog over the northwestern Pacific Ocean. ICOADS provides surface meteorological observations from ships and buoys over the global ocean. Specifically, surface air temperature (SAT), 10 m wind speed, visibility and SST are used to identify sea fog occurrence and characterize the associated air–sea conditions.

We use the Moderate Resolution Imaging Spectroradiometer (MODIS) visible imagery to delineate the spatial extent of sea fog (Platnick et al., 2003). We further use MODIS retrieval products, including LWP, cloud optical thickness (τ_c), and cloud droplet effective radius (r_e), to characterize the fog layer and infer its microphysical properties. These variables are then used to estimate the cloud droplet number concentration (N_d) in sea fog according to

https://doi.org/10.5194/egusphere-2026-2980
Preprint. Discussion started: 13 July 2026

$$N_d = \frac{\sqrt{5}}{2\pi k}\left(\frac{f_{ad} c_w \tau_c}{Q_{ext} \rho_w r_e^5}\right)^{\frac{1}{2}}, \quad (1)$$

where k is the ratio of the volume-mean radius to the effective radius of cloud droplets, f_{ad} is the adiabatic fraction, c_w is the vertical gradient of liquid water content, Q_{ext} is the extinction efficiency, and ρ_w is the density of liquid water (Grosvenor et al., 2018).

The fifth-generation reanalysis dataset from the European Centre for Medium-Range Weather Forecasts (ERA5; Hersbach et al., 2020) is used to construct the initial conditions for the LESs, including temperature, specific humidity, geopotential height, and wind fields. ERA5 provides hourly data at a horizontal resolution of 0.25° × 0.25°, with 7 pressure levels at and below 850 hPa. The Modern-Era Retrospective analysis for Research and Applications, Version 2 (MERRA-2; Gelaro et al., 2017) is a widely used global atmospheric reanalysis dataset that provides a variety of aerosol variables. We use the mass mixing ratios of different aerosol components from MERRA-2 to constrain the initial aerosol conditions in the model. We followed Grainger (2012) to convert aerosol mass mixing ratios to number mixing ratios.

2.2 UCLALES–SALSA model

UCLALES is a three-dimensional boundary-layer model with turbulence closure, in which the prognostic variables include total water mixing ratio, liquid water potential temperature, and the three wind components (Stevens et al., 2005). Subgrid-scale turbulence is parameterized using the Smagorinsky–Lilly scheme (Lilly, 1967). Radiative transfer is calculated using the δ–four-stream approximation (Fu and Liou, 1993). UCLALES uses prescribed SST to calculate surface momentum, heat, and moisture fluxes. A damping layer at the top of the domain suppresses spurious gravity waves. UCLALES has previously been shown to reproduce the evolution of sea fog (Yang et al., 2021, 2024).

UCLALES–SALSA couples UCLALES, which resolves atmospheric boundary-layer dynamics (Stevens et al., 2005), with the sectional aerosol–cloud microphysics module SALSA (Kokkola et al., 2008; Tonttila et al., 2017). SALSA employs a spectral bin representation to predict the number and mass mixing ratios of aerosol particles, cloud droplets, and precipitation particles (Kokkola et al., 2008). The scheme explicitly resolves key microphysical processes, including condensation, evaporation, collision–coalescence, and droplet activation. In contrast to bulk microphysics schemes, droplet activation is derived from particle growth trajectories without relying on empirical CCN parameterizations (Tonttila et al., 2017). Because the droplet size distribution is explicitly resolved, UCLALES–SALSA can calculate droplet terminal fall velocities and directly diagnose the sedimentation flux of cloud and fog droplets. The model has been extensively

https://doi.org/10.5194/egusphere-2026-2980
Preprint. Discussion started: 13 July 2026

evaluated in simulations of liquid-phase clouds and fog (Boutle et al., 2018; Calderón et al., 2022).

2.3 Model configuration

The model configuration was based largely on that used by Yang et al. (2021, 2024), with several modifications introduced for the present case. The UCLALES–SALSA simulations were conducted in a domain of 3000 m × 3000 m × 2000 m, with a horizontal grid spacing of 150 m. The vertical grid spacing was 5 m below 200 m and increased exponentially above this height with an *e*-folding factor of 1.1. An adaptive time-stepping scheme was used, with a maximum time step of 1 s.

To represent the evolution of a sea-fog air column from a Lagrangian perspective, the air-column trajectory was first reconstructed using the Hybrid Single-Particle Lagrangian Integrated Trajectory model. As shown in Fig. 2, a fog observation at 49.6° N, 183.2° E at 00:00 UTC on July 4, 2013 was selected, and the corresponding backward trajectory was traced to identify the upstream pathway of the fog air column. The starting point of the simulation was located at 42.3° N, 148.34° E at 00:00 UTC on June 30, 2013.

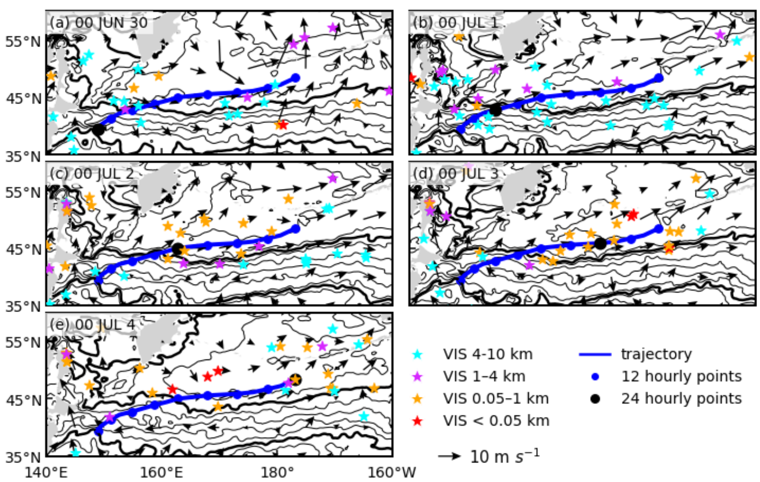

Figure 2. ICOADS and ERA5 observations, and the backward trajectory of the advection fog event during June 30–July 4, 2013. (a)–(e) correspond to 12:00 UTC on June 30, July 1, July 2, July 3, and July 4, respectively. The blue line denotes the 4 d backward trajectory initialized from a fog observation at 49.6° N, 183.2° E at 12:00 UTC on July 4, while blue dots mark the trajectory position every 12 h and the larger black dot indicates the trajectory location at the time of each panel. Colored stars indicate fog observations with different visibility levels. Contours show ERA5 SST averaged over June 30–July 4 with a 2 °C interval; and thick contours denote 10, 20, and 30 °C.

The initial thermodynamic structure was derived from ERA5 reanalysis. Vertical profiles of potential temperature and specific humidity were first obtained from ERA5, and the initial inversion height was determined jointly from ERA5 temperature profiles. The initial atmosphere was then idealized into three layers, namely a mixed layer, an inversion

https://doi.org/10.5194/egusphere-2026-2980
Preprint. Discussion started: 13 July 2026

layer, and the free troposphere (Fig. A1). Within the 400 m deep mixed layer, potential temperature (θ) and total water mixing ratio (r_t) were assumed to be vertically uniform (Figs. A1a and A1b). Above the mixed layer, an inversion with a 6 K jump in θ was prescribed. In the free troposphere, θ and r_t decreased with height at rates of 6.6 K km^{-1} and 2.8 g kg^{-1} km^{-1}, respectively. A geostrophic wind speed of 9.6 m s^{-1} was prescribed throughout the simulation.

The model was driven by prescribed lower-boundary and large-scale forcing along the reconstructed trajectory. SST varied with time and was specified from observations along the air-column pathway. To simplify the forcing, the observed SST evolution during the first 36 h was fitted with a cosine function, followed by a constant value of 8 °C thereafter. Large-scale divergence was prescribed as a constant value of 4 × 10^{-6} s^{-1} throughout the simulation. In the control experiment, the solar elevation angle was prescribed as a function of latitude, longitude, and time to represent the diurnal cycle of solar insolation.

The initial aerosol population was prescribed as a bimodal lognormal distribution, with its vertical structure constrained by MERRA-2 (Gelaro et al., 2017). MERRA-2 aerosol data of sulfate and sea salt were extracted along the trajectory and vertically averaged over the initial period to constrain the initial aerosol population. The Aitken mode number concentration was fixed at 1000 cm^{-3}, with a geometric mean diameter of 50 nm and a geometric standard deviation of 1.4. The accumulation mode varied with height: its number concentration was set to 600 cm^{-3} at the sea surface, decreased linearly to 300 cm^{-3} at the mixed-layer top, increased to 375 cm^{-3} within the inversion layer, and remained constant above (Fig. A1). The accumulation mode was assigned a geometric mean diameter of 200 nm and a geometric standard deviation of 1.6. Aerosol particles were assumed to be internally mixed and composed primarily of sulfate and sea salt.

Aerosol and fog-droplet bins were defined in terms of dry diameter, while the corresponding wet diameters were calculated prognostically. In the present simulations, SALSA was configured with 15 size bins for aerosol particles and 12 size bins for fog droplets generated from each aerosol regime. To represent aerosol evolution, sea-salt emissions from the ocean surface were introduced after 7.5 h of simulation time following Berner et al. (2013). The emitted sea-salt particles were represented by a single lognormal mode with a geometric mean diameter of 0.26 μm, a geometric standard deviation of 2, and a total number emission rate of

$$\frac{dN}{dt} = 1.706 \times 10^2 u_{10}^{3.14}, \quad (2)$$

where the 10 m wind speed, u_{10}, was set to 9.6 m s^{-1}.

https://doi.org/10.5194/egusphere-2026-2980
Preprint. Discussion started: 13 July 2026

2.4 Experimental design

To investigate the role of gravitational droplet sedimentation in advection fog evolution, a set of numerical experiments was conducted based on the same model configuration. The control (CTRL) experiment prescribed the solar elevation angle as a function of latitude, longitude, and time along the reconstructed trajectory, thereby representing the realistic diurnal variation in solar insolation. A second experiment, denoted as NoDiurnal, was performed with the solar elevation angle fixed in time in order to eliminate the effect of the diurnal cycle of solar radiation.

Based on the NoDiurnal setup, two aerosol-sensitivity experiments, HighAero and LowAero, were further conducted by multiplying or dividing the accumulation-mode aerosol number concentration by 3, respectively. In addition, NoCollCoal and NoSedi experiments were conducted by disabling droplet collision–coalescence and gravitational sedimentation, respectively.

2.5 Liquid water path budget

Following Wærsted et al. (2018), the modelled LWP tendency was decomposed into contributions from individual physical processes to evaluate their relative roles in the fog life cycle. Specifically, the LWP tendency was expressed as,

$$\frac{dLWP}{dt} = F_{rad} + F_{sedi} + F_{SH} + F_{LH} + F_{turb} + F_{ent} + F_{sub}, \quad (3)$$

where F_{rad}, F_{sedi}, F_{SH}, F_{LH}, F_{turb}, F_{ent}, and F_{sub} denote the contributions from radiation, fog-base sedimentation, sensible heat flux, latent heat flux, fog-base turbulent transport, entrainment, and large-scale subsidence, respectively. The detailed formulations of these budget terms and associated fluxes are provided in Appendix B.

3. Synoptic processes and satellite observations

We examine an advection fog event over the northwestern Pacific during July 1–4, 2013. A strong SST gradient was present between 38 and 45° N (Fig. 2). The event developed under the influence of a high-pressure system centered southeast of the fog trajectory, near 35–40° N and 180–190° E (not shown). During July 1–4, near-surface southwesterly winds prevailed over the SST frontal region, advecting warm, moist air over the colder ocean surface and thereby favoring advection-fog formation (Figs. 2b–e). Visibility below 4 km was first reported near the Kuril Islands on June 30 (Fig. 2a). As the saturated air mass moved northeastward, visibility within the fog patch decreased to below 1 km during July 2–4 (Figs. 2b–d). By 00:00 UTC on July 4, observations with visibility exceeding 1 km appeared within the fog area, indicating the dissipation of the fog (Fig. 2e). More details of this event are provided in Yang et al. (2021, 2024).

https://doi.org/10.5194/egusphere-2026-2980
Preprint. Discussion started: 13 July 2026

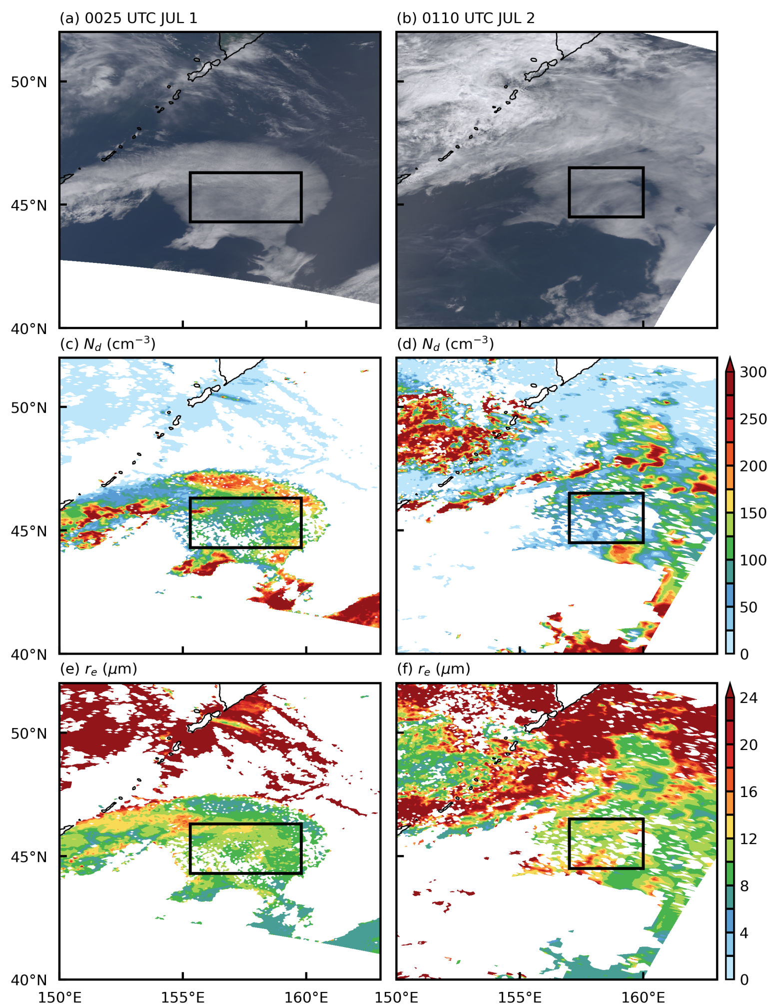

Figure 3. MODIS visible images at 00:25 UTC on July 1 (a) and 01:10 UTC on July 2 (b). (c) (d), and (e) (f) show the corresponding MODIS-retrieved cloud droplet number concentration (cm^{-3}), and cloud droplet effective radius (μm), respectively. The black boxes denote the regions used to sample fog properties for constructing the probability distributions shown in Fig. S1.

MODIS observations futher characterize the fog microphysics. The visible imagery shows a spatially homogeneous gray–white region west of the Kuril Islands, with smooth boundaries and little internal texture (black boxes in Figs. 3a and 3b), suggesting the presence of sea fog. Comparison between the two satellite images indicates northwestward movement of the fog patch. Figures 3c and 3d show the N_d retrieved from Eq. (1). On July 1, N_d within the fog patch was generally higher than 80 cm^{-3}. On July 2, however, N_d decreased to approximately 50 cm^{-3}, indicating a pronounced reduction in fog droplet number concentration. This decrease in N_d is further confirmed by the frequency

https://doi.org/10.5194/egusphere-2026-2980
Preprint. Discussion started: 13 July 2026

distributions within the selected region (Fig. S1a), which show a shift in the modal N_d from 80–120 cm^{-3} on July 1 to 60–80 cm^{-3} on July 2.

The distribution of cloud optical depth (τ_c) shifted toward lower values, with the peak decreasing from 6–7 on July 1 to 4–5 on July 2 (Fig. S1b). At the same time, the effective radius (r_e) shifted toward larger sizes, with the peak increasing from 8–10 µm to 10–12 µm, indicating droplet growth (Fig. S1c and Figs. 3e and 3f). The distribution of LWP also moved toward lower values, with the peak frequency shifting from 30–40 g m^{-2} on July 1 to 20–30 g m^{-2} on July 2, accompanied by a pronounced reduction in the occurrence of LWP values above 50 g m^{-2} (Fig. S1d). Overall, from July 1 to 2, the fog exhibits a coherent evolution characterized by decreasing N_d, τ_c, and LWP and increasing r_e. These features indicate a reduction in fog droplet number accompanied by droplet growth and a decrease in total liquid water content.

4. Simulated fog evolution and sedimentation processes

4.1 Control simulation and comparison with observations

Figure 4 presents the simulated evolution of the fog along the trajectory in the CTRL run. UCLALES-SALSA successfully reproduces a fog layer forming at around 12:00 UTC on June 30, with a clear diurnal variation. In the first ~4 h after formation, the fog layer deepens rapidly and the LWC increases markedly, whereas the liquid water decreases during the daytime (Fig. 4a). This nocturnal enhancement and daytime dissipation of the fog layer repeat over the subsequent three days.

The visibility was diagnosed from liquid water content following Kunkel (1984)

$$VIS = -\frac{\ln(\epsilon)}{\beta}, \quad (4)$$

where ϵ = 0.02 and β = 144.7·LWC$^{0.88}$. The resulting LWC-derived visibility compares reasonably well with the observed visibility along the fog trajectory (Fig. 4b), with lower values at night and higher values during the daytime. In addition, the simulated surface air temperature (SAT) falls below the SST when the solar elevation angle is low after 12:00 UTC on July 1. These results indicate that LRC at the fog top is an important driver of fog evolution, while daytime shortwave radiative heating partly offsets this cooling effect. This mechanism has been documented in previous studies (Yang et al., 2024; Yang and Gao, 2020). As a result, the fog tends to exhibit higher LWC and lower visibility at night.

https://doi.org/10.5194/egusphere-2026-2980
Preprint. Discussion started: 13 July 2026

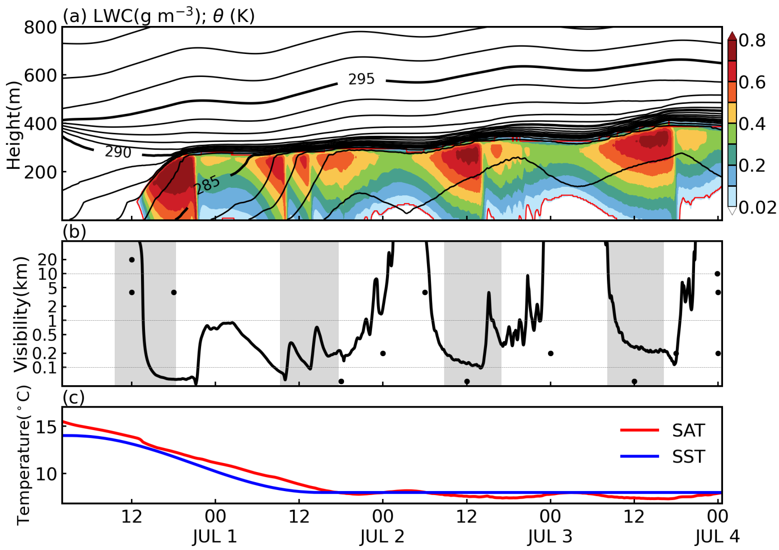

Figure 4. (a) Time–height section of simulated liquid water content (shading, g m^{-3}) and potential temperature (contours, interval 1 K) for CTRL experiment. Red lines indicate the fog/cloud top and bottom, defined by the contour of LWC 0.02 g m^{-3}. (b) Simulated visibility (line, km) and ICOADS observed visibility sampled along the trajectory shown in Fig. 2 (dots, km). The ICOADS observations were selected within ±2 h of each trajectory time and within ±2° latitude/longitude of the corresponding trajectory position. The gray shading indicates nighttime. (c) SAT (red line, °C) and SST (blue line, °C).

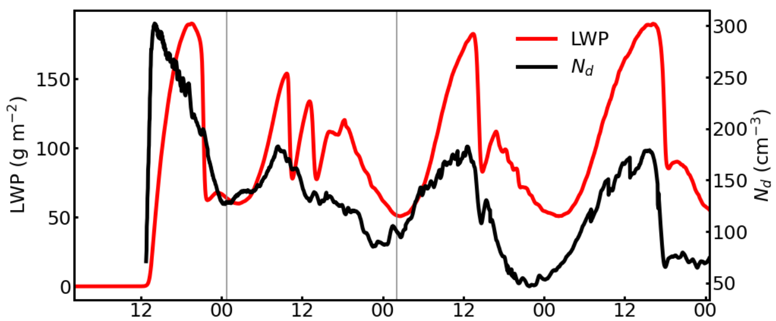

Figure 5. Time series for the CTRL experiment: liquid water path (red line, g m^{-2}) and mean droplet number concentration within 100 m below the fog top (black line, cm^{-3}). The gray vertical lines indicate the time of the MODIS observations shown in Fig. 3.

Figure 5 shows the evolution of the simulated LWP and the fog-top N_d averaged over the uppermost 100 m of the fog layer. The fog top was determined using the LWC threshold of 0.016 g m^{-3}. Both quantities exhibit pronounced diurnal variations and broadly follow the trends inferred from MODIS. Specifically, the simulated LWP decreases from approximately 63 g m^{-2} at 00:25 UTC on July 1 to 51 g m^{-2} at 01:10 UTC on July 2, while N_d decreases from about 128 to 100 cm^{-3} over the same period. Given the strong diurnal variability in both variables, however, these decreasing tendencies cannot be attributed solely to microphysical processes within the fog layer. They may also reflect changes in

https://doi.org/10.5194/egusphere-2026-2980
Preprint. Discussion started: 13 July 2026

the radiative balance near the fog top associated with variations in solar radiation. The simulated LWP and N_d are slightly higher than their MODIS-derived counterparts, which may be partly related to uncertainties in the thermodynamic stratification prescribed by the reanalysis data, as well as uncertainties inherent in satellite retrievals (Grosvenor et al., 2018; Gryspeerdt et al., 2022). Overall, UCLALES–SALSA reasonably reproduces the formation and temporal evolution of this sea-fog event.

4.2 Fog evolution in the NoDiurnal experiment

Given that the CTRL run reasonably reproduces the observed evolution of the sea fog, we further conduct an LES experiment with a constant solar elevation to exclude the influence of diurnal variation, referred to as the NoDiurnal run. The simulated results during the first ~4 h are broadly similar to those in the CTRL run, except that the LWC in the NoDiurnal run is slightly higher. After this initial period, the near-surface LWC decreases from more than 0.3 g m^{-3} to less than 0.1 g m^{-3}. Correspondingly, the visibility increases from about 0.1 km and then fluctuates within the range of 0.5–1 km.

A notable difference from previous studies is that the near-surface LWC in the present NoDiurnal run, typically below 0.1 g m^{-3}, is markedly lower than that reported in earlier LES studies without an explicit microphysics scheme (e. g., Yang et al., 2021, 2024). This difference is likely related to the frequent sedimentation of fog droplets from the fog top, which contributes to the relatively low near-surface LWC. This process is manifested by intermittent downward-extending streak-like features from the fog top toward the fog base (Figs. 4a and 6a).

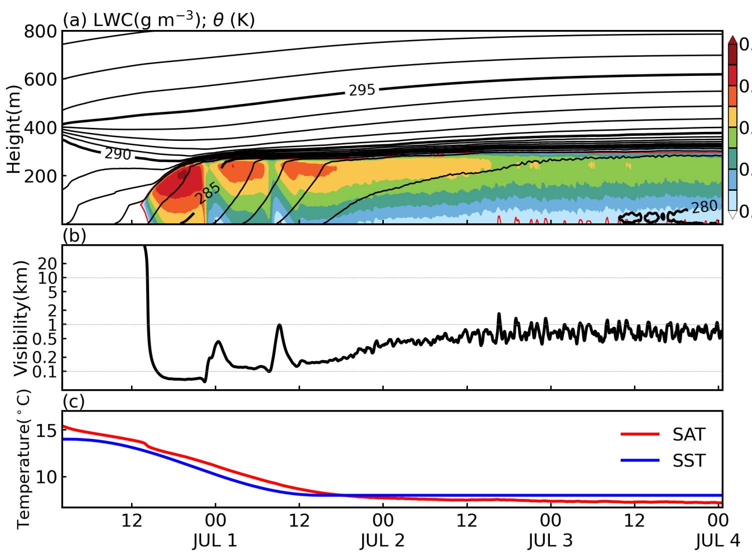

Figure 6. As in Fig. 4 but for the NoDiurnal experiment.

https://doi.org/10.5194/egusphere-2026-2980
Preprint. Discussion started: 13 July 2026

4.3 Microphysical signatures of droplet sedimentation

The sedimentation of fog droplets is more evident in the liquid water sedimentation flux shown in Fig. 7c. Prior to 10:00 UTC on June 1, two pronounced sedimentation events occur, with fluxes exceeding 75 g m^{-2} h^{-1} and extending vertically from the fog top to the fog base. These events are linked to the gradual increase in effective radius near the fog top and the concurrent decrease in N_d (Fig. 7a), suggesting that the formation of larger droplets promotes gravitational settling during this period (Fig. 7b). Thereafter, sedimentation becomes weaker but occurs more frequently. The marked reduction in sedimentation flux below 50 m indicates that a substantial fraction of the settling droplets evaporates before reaching the surface.

An associated feature is the rapid depletion of aerosol particles within the fog layer (Fig. 7d). The aerosol number concentration decreases from approximately 1400 to 700 cm^{-3} within 3 h after fog formation, consistent with recent aerosol observations during sea-fog events (Fernando et al., 2025; Zhao et al., 2022). This rapid aerosol depletion indicates efficient removal of potential cloud condensation nuclei through activation, condensational growth, and subsequent sedimentation of fog droplets. It also implies that the subsequent evolution of the fog layer may become sensitive to the availability of cloud condensation nuclei, highlighting the potential importance of sea-salt aerosol emissions in sustaining the aerosol population within the sea-fog layer.

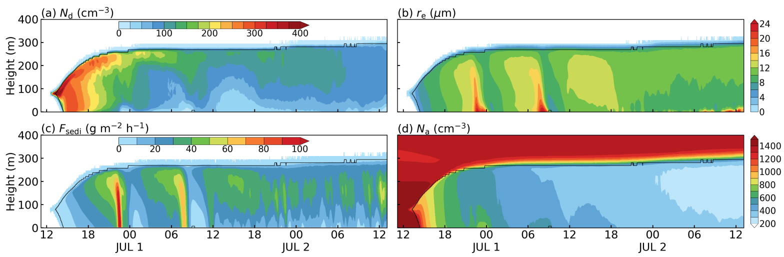

Figure 7. Time-height sections of microphysical properties for the NoDiurnal experiment: (a) Cloud droplet number concentration (cm^{-3}), (b) effective radius (μm), (c) sedimentation flux (g m^{-2} h^{-1}), and (d) aerosol number concentration (cm^{-3}). Black line indicates the fog top.

The time series of r_e and the sedimentation fluxes at the fog top and base indicate a close temporal relationship among these variables (Fig. 8a). To quantify this relationship, we perform a lead–lag correlation analysis (Fig. 8b). Because the two sedimentation events before 10:00 UTC on June 1 are exceptionally strong and may disproportionately affect the correlation estimates, the Spearman rank correlation coefficient is used instead of Pearson correlation.

https://doi.org/10.5194/egusphere-2026-2980
Preprint. Discussion started: 13 July 2026

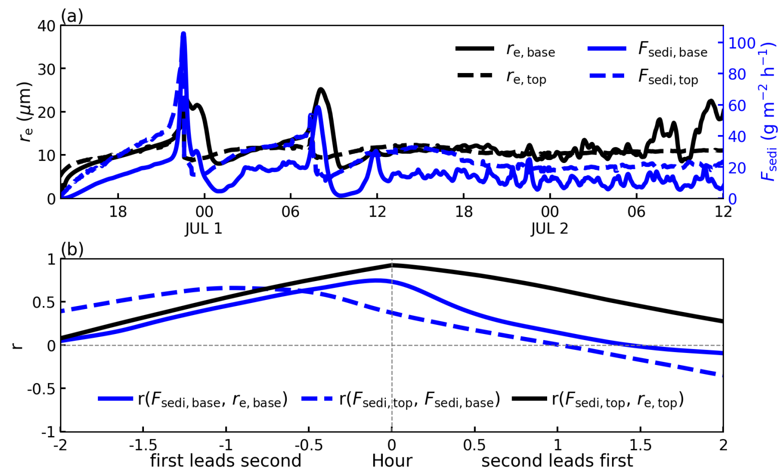

Figure 8. (a) Time series of effective radius r_e and liquid water sedimentation flux F_{sedi} at the fog base and fog top in the NoDiurnal experiment. Black lines denote r_e (μm), and blue lines denote F_{sedi} (g m^{-2} h^{-1}); solid and dashed lines indicate values at the fog base and fog top, respectively. (b) Lead–lag Spearman correlation coefficients for $F_{sedi,base}$ versus $r_{e,base}$ (solid blue line), $F_{sedi,top}$ versus $F_{sedi,base}$ (dashed blue line), and $F_{sedi,top}$ versus $r_{e,top}$ (solid black line). Positive lags, corresponding to the right-hand side of the x axis, indicate that the second variable leads the first; negative lags indicate that the first variable leads the second. The lead–lag correlations were computed using data from 14:00 UTC on June 30 to 12:00 UTC on July 2.

At the fog top, the correlation between sedimentation flux and r_e reaches its maximum at zero time lag, suggesting that the two variables vary nearly synchronously. The sedimentation flux at the fog top leads its fog-base counterpart by approximately 1 h, implying that the sedimentation signal requires about 1 h to reach the fog base. Given a mean fog-top height of about 280 m, this time lag yields an approximate mean sedimentation velocity of 7.7 cm s^{-1}. Using Stokes' law, this velocity corresponds to a fog-droplet radius of approximately 25 μm. This estimate should be interpreted as an effective sedimentation radius, since it neglects turbulence, vertical variations in droplet size, and evaporation during descent. In addition, the sedimentation flux at the fog base leads r_e by about 10 min, suggesting that sedimentation contributes to the subsequent marked increase in droplet effective radius near the fog base.

Figure 9 further illustrates the vertical propagation characteristics of sedimentation associated with fog-top droplet growth. The strongest positive correlations between the sedimentation flux and fog-top effective radius ($r_{e,top}$) occur in the upper fog layer at positive lags close to 0–1 h. The correlation maximum subsequently extends downward with increasing lag, suggesting a downward propagation of the sedimentation signal from the fog top toward the lower fog layer. These results support the interpretation that droplet growth near the fog top promotes gravitational settling and links fog-top liquid-water production to delayed liquid-water removal below.

https://doi.org/10.5194/egusphere-2026-2980
Preprint. Discussion started: 13 July 2026

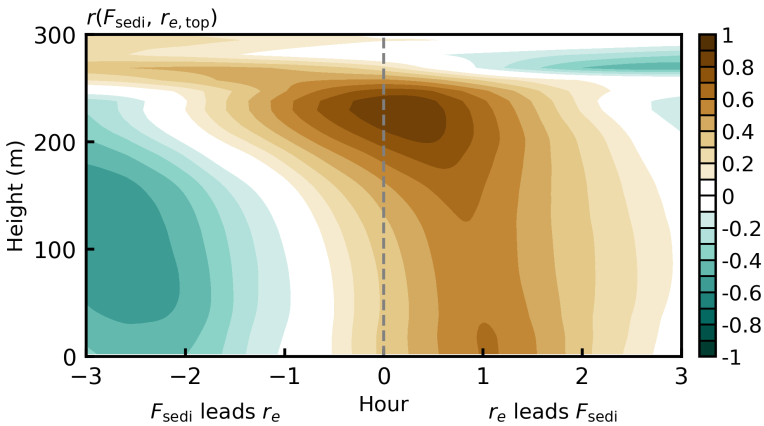

Figure 9. Lead–lag Spearman correlation coefficients between liquid water sedimentation flux, F_{sedi}, at each height and effective radius at fog top, $r_{e,top}$ in the NoDiurnal experiment. Positive lags, corresponding to the right-hand side of the x axis, indicate that r_e leads the sedimentation flux; negative lags indicate that the sedimentation flux leads r_e. The lead–lag correlations were computed using data from 14:00 UTC on June 30 to 12:00 UTC on July 2.

4.4 Liquid-water budget analysis

The liquid water budget clarifies the processes controlling the vertical evolution of the fog layer (Fig. 10). During the initial growth stage, condensation is the dominant source of liquid water and produces positive tendencies through a deep portion of the fog layer (Figs. 10a and 10b), reflecting the rapid adjustment of the near-saturated boundary layer after fog formation. As the fog layer deepens and becomes optically thicker, the condensation tendency becomes increasingly concentrated near the fog top, consistent with the development of strong fog-top LRC that maintains local supersaturation near the upper boundary of the fog layer. Turbulent mixing acts mainly as a redistribution process rather than a net liquid-water source: it transports fog-top-produced liquid water downward into the fog interior (Fig. 10c).

Sedimentation provides another important pathway for transporting liquid water downward from the fog top (Fig. 10d). The negative sedimentation tendency near the fog top, together with the positive tendencies below, indicates that droplets formed or grown near the fog top settle gravitationally and transfer liquid water toward lower levels. The size-resolved sedimentation tendencies further show that this downward transport is mainly associated with droplets with radii larger than 10 μm (Fig. 10f). In contrast, the sedimentation tendency associated with droplets with radii smaller than 10 μm is more scattered and less physically coherent (Fig. 10g), likely reflecting intrinsic numerical limitations of the bin microphysics scheme. The residual term remains relatively small compared with the main budget terms, indicating that the dominant physical tendencies are well captured (Fig. 10e).

https://doi.org/10.5194/egusphere-2026-2980
Preprint. Discussion started: 13 July 2026

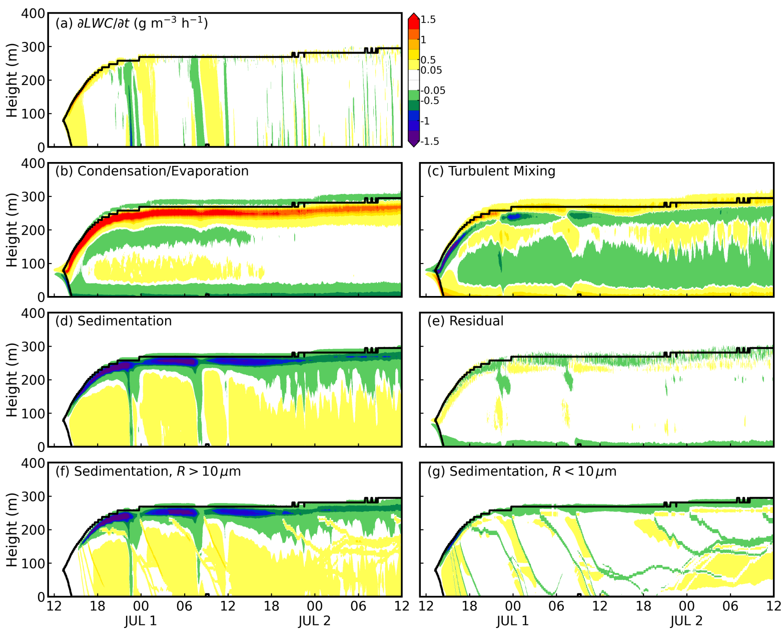

Figure 10. Time-height sections of the budget terms for LWC (g m^{-3} h^{-1}) for the NoDiurnal experiment: (a) total tendency of LWC, (b) contribution from condensation/evaporation, (c) contribution from turbulent mixing, (d) contribution from sedimentation, (e) residual term, (f) sedimentation from droplets with radius > 10 μm, and (g) sedimentation from droplets with radius < 10 μm. Black lines indicate the fog/cloud top and bottom.

Previous studies have identified a positive feedback between fog-top LRC and liquid-water production: radiative cooling enhances condensation near the fog top, while the resulting liquid-water accumulation further strengthens radiative cooling (Mazoyer et al., 2017; Yang et al., 2021, 2024; Yang and Gao, 2020). The present budget analysis further suggests that sedimentation provides an additional microphysical pathway transporting fog-top-generated liquid water downward. In this way, droplet sedimentation may weaken the radiative–condensational positive feedback by limiting the local increase in fog-top LWC and the associated enhancement of LRC. This interpretation is consistent with the gradual weakening of the condensation tendency near the fog top (Fig. 10b). Thus, sedimentation is not merely a sink or redistribution term, but a potentially important regulator of fog-top radiative feedback.

To complement the vertically resolved liquid water budget, we further diagnose the LWP budget following Wærsted et al. (2018), in which the time tendency of LWP is attributed to individual physical processes (Appendix B). Figure 11 shows the mean LWP budget during the sea fog in the NoDiurnal run. The dominant positive contribution comes from the radiation term, reaching about 30 g m^{-2} h^{-1}. This indicates that condensation induced by fog top LRC is the primary process responsible for liquid water production and

https://doi.org/10.5194/egusphere-2026-2980
Preprint. Discussion started: 13 July 2026

maintenance within the fog layer (Figs. 10b and 11). In contrast, sedimentation at the fog base is the largest negative contribution (~−20 g m^{-2} h^{-1}), suggesting that droplet sedimentation continuously removes liquid water from the base of the fog layer and suppresses LWP accumulation (Fig. 11).

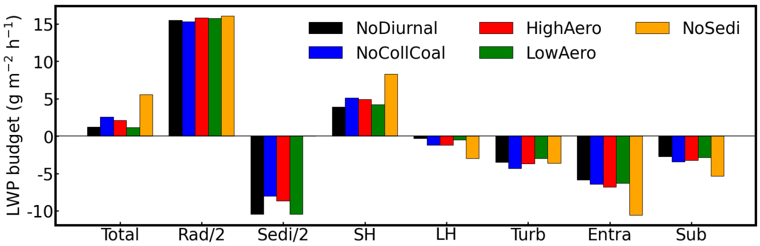

Figure 11. Bars of LWP budget terms (g m^{-2} h^{-1}) including total tendency, radiation, sedimentation, sensible heat, latent heat, turbulent mixing, entrainment, and subsidence. Radiation and sedimentation have been multiplied by factor of 0.5 to fit in the same scale. The LWP budget terms were averaged over the period from 12:00 UTC on June 30 to 00:00 UTC on July 3.

In addition, the sensible heat term associated with the air–sea temperature difference provides a positive contribution of 4 g m^{-2} h^{-1} (Fig. 11). The latent heat term, turbulent liquid water transport near the fog base, fog top entrainment, and subsidence act as LWP loss terms, partly offsetting the liquid water increase driven by radiative cooling and sea surface cooling.

Overall, the liquid-water and LWP budgets consistently show that fog-top radiative cooling is the primary source of liquid water, whereas gravitational sedimentation is the dominant microphysical sink. This balance indicates that sedimentation plays a central role in regulating LWP accumulation and moderating the radiative–condensational feedback during the evolution of advection fog.

5. Sensitivity experiments

To assess the robustness of the sedimentation effect, we further examine the NoSedi, NoCollCoal, HighAero, and LowAero experiments. The most pronounced response occurs in the NoSedi experiment (Fig. 12a). Compared with the NoDiurnal experiment, switching off gravitational sedimentation leads to a substantial accumulation of liquid water throughout the fog layer, with near-surface LWC exceeding 0.4 g m^{-3}. This confirms that droplet sedimentation is a major process limiting excessive liquid water in the model; when this sink is removed, the simulated fog becomes much denser, as also reflected by the enhanced total LWP tendency in Fig. 11.

However, the LWP increase caused by disabling droplet sedimentation is partly offset by stronger cloud-top entrainment and large-scale subsidence (Fig. 11). More importantly, the impact of sedimentation is not confined to liquid-water removal near the fog base. By

https://doi.org/10.5194/egusphere-2026-2980
Preprint. Discussion started: 13 July 2026

00:00 UTC on July 4, the fog/cloud top in NoSedi is approximately 270 m higher than in NoDiurnal (Fig. 12d), indicating that sedimentation also regulates the vertical development of the fog layer. This behavior is consistent with recent observational and super-droplet modeling studies (Yang et al., 2025; Yin et al., 2024), which suggest that cloud-top droplet sedimentation can modify the vertical distribution of liquid water and thereby influence cloud-top entrainment processes.

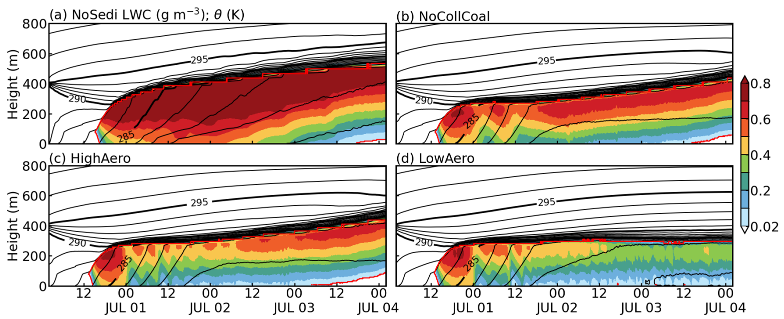

Figure 12. As in Fig. 6a but for the: (a) NoSedi, (b) NoCollCoal, (c) HighAero, and (d) LowAero experiments. Red lines indicate the fog/cloud top and bottom.

The NoCollCoal experiment also shows a clear response, although the change in fog structure is less pronounced than in NoSedi (Figs. 11 and 12c). Compared with NoDiurnal, switching off collision–coalescence approximately doubles the total LWP tendency. This increase is mainly caused by a reduced sedimentation loss, with F_{sedi} decreasing in magnitude from approximately -20 to -16 g m^{-2} h^{-1} (Fig. 11 and Fig. S2b). In contrast, the radiation term changes only weakly, indicating that the enhanced LWP tendency primarily results from weakened liquid-water removal rather than increased radiative production. In NoCollCoal, the fog/cloud top rises faster than in NoDiurnal but more slowly than in NoSedi, eventually leading to the dissipation of near-surface fog at around 14:00 UTC on July 3 (Fig. 12b). The cloud water structure in NoCollCoal remains broadly similar to that in NoDiurnal, but with somewhat larger liquid-water amounts in the fog layer (Fig. 12c). These results suggest that collision–coalescence contributes to the formation of larger droplets and thereby enhances sedimentation, but it is not the dominant process controlling the overall vertical development of the fog layer.

The aerosol-sensitivity experiments further show that aerosol loading modulates the sedimentation effect by regulating droplet size (Figs. 12c and 12d). In the HighAero experiment, the larger aerosol concentration leads to more numerous but smaller droplets, thereby weakening gravitational settling and allowing more liquid water to remain in the fog layer (Fig. 12c, Fig. S2c and Fig. S3c). Consequently, the fog/cloud top rises slightly faster than in NoDiurnal, and near-surface fog persists until the end of the analyzed period.

https://doi.org/10.5194/egusphere-2026-2980
Preprint. Discussion started: 13 July 2026

In contrast, the LowAero experiment produces fewer but larger droplets, which enhances sedimentation and suppresses liquid-water accumulation (Fig. 12d, Fig. S2d and Fig. S3d). The fog/cloud top remains lower, and the fog layer is thinner than in HighAero. These differences indicate that aerosol concentration controls the efficiency of sedimentation by shifting the droplet size distribution.

Figure 13 further illustrates how the microphysical perturbations modify the fog droplet size distribution at fog base. In the NoDiurnal experiment, the droplet spectrum frequently exhibits a bimodal structure, consisting of a small-droplet mode associated with newly activated droplets and a large-droplet mode associated with sedimenting droplets (Fig. 13a). The large-droplet tail extending beyond 10 μm is particularly important, because droplets in this size range contribute disproportionately to sedimentation flux owing to their much larger fall velocities, consistent with the enhanced sedimentation efficiency shown in Fig. 10f. The bimodal structure becomes less pronounced in the NoCollCoal and HighAero experiments, where suppressed collision–coalescence or enhanced aerosol loading limits droplet growth and reduces the occurrence of droplets larger than 10 μm. In contrast, the LowAero experiment exhibits a more distinct large-droplet mode, consistent with enhanced droplet growth and stronger sedimentation.

The origin of the bimodal fog-droplet spectrum remains uncertain, and several physical mechanisms have been proposed, including evaporation–recondensation cycles, collision–coalescence, and Ostwald ripening. The UCLALES–SALSA simulations suggest that collision–coalescence tends to weaken the bimodal structure near the fog base, although the physical mechanism responsible for this behavior remains unclear and requires further investigation.

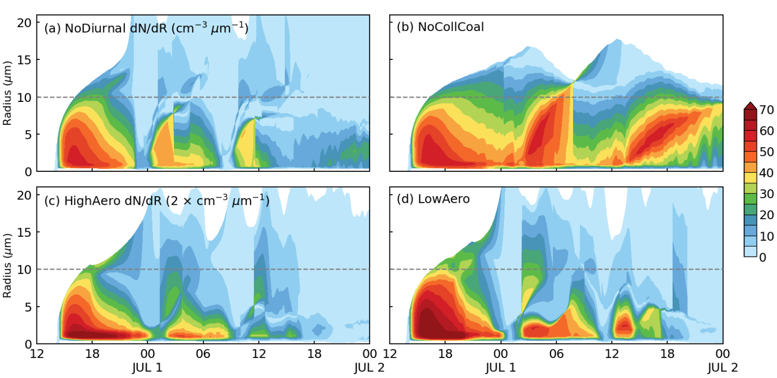

Figure 13. Time-radius distributions of fog droplet number concentration (cm^{-3} μm^{-1}) at fog base for the: (a) NoDiurnal, (b) NoCollCoal, (c) HighAero, and (d) LowAero experiments. Values for the HighAero experiment are scaled by 0.5 to fit the common color scale.

https://doi.org/10.5194/egusphere-2026-2980
Preprint. Discussion started: 13 July 2026

Overall, the sensitivity experiments confirm that gravitational sedimentation is a key regulator of advection-fog evolution. Removing sedimentation produces excessive liquid-water accumulation and a much deeper fog/cloud layer, demonstrating its dominant role as a microphysical sink. Collision–coalescence also contributes by promoting larger droplets and enhancing sedimentation, while aerosol concentration modulates the sedimentation efficiency through its control on droplet size. These results indicate that realistic treatment of droplet sedimentation and its microphysical controls is essential for simulating the liquid-water content and vertical structure of advection fog.

6. Summary and discussion

This study investigates how gravitational droplet sedimentation regulates liquid water in marine advection fog using large-eddy simulations with the sectional aerosol–cloud microphysics model UCLALES–SALSA (University of California, Los Angeles Large-Eddy Simulation model coupled with the Sectional Aerosol module for Large Scale Applications). The coupling between UCLALES and SALSA enables a detailed representation of turbulence, radiation, and aerosol–cloud microphysical processes within the fog layer. A typical advection-fog event over the northwestern Pacific during June 30–July 4, 2013 was simulated from a Lagrangian perspective. The results reveal that droplet sedimentation acts not only as a liquid-water sink but also as a vertically coupled microphysical process that regulates liquid-water redistribution and fog-layer development.

UCLALES–SALSA reasonably reproduces the observed evolution of the sea-fog event. In the CTRL experiment, the model captures the formation of a shallow fog layer after the air column crosses the SST front, as well as the subsequent diurnal variations in liquid water and visibility (Figs. 3 and 4). The simulated LWP and fog-top droplet number concentration are broadly consistent with MODIS retrievals, although both are slightly higher than the satellite-derived estimates. The model also reproduces the observed tendency toward decreasing droplet number concentration and increasing effective radius from July 1 to July 2, indicating that UCLALES–SALSA captures the main microphysical evolution of the fog layer. This agreement supports the use of the simulations for examining the role of droplet sedimentation in the subsequent process analysis.

Building on this model evaluation, the NoDiurnal experiment was used to isolate the sedimentation-related processes from the influence of diurnal solar forcing. In this experiment, the near-surface LWC decreases from more than 0.3 to less than 0.1 g m^{-3} after the initial growth stage, indicating substantial liquid-water removal from the lower fog layer (Fig. 6). Large droplets form preferentially near the fog top (Fig. 7b), where longwave

https://doi.org/10.5194/egusphere-2026-2980
Preprint. Discussion started: 13 July 2026

radiative cooling maintains liquid-water production (Fig. 10b), and their subsequent settling produces intermittent downward sedimentation signals from the fog top toward the fog base, with peak sedimentation fluxes exceeding 75 g m^{-2} h^{-1}. The lead–lag correlation analysis (Fig. 9) further shows that the fog-top sedimentation signal leads the fog-base signal by approximately 1 h, corresponding to an effective sedimentation velocity of about 7.7 cm s^{-1} and an effective droplet radius of approximately 25 μm. These results indicate that sedimentation limits the accumulation of liquid water near the fog top, redistributes liquid water vertically, and contributes to the relatively low near-surface liquid-water amount simulated in this experiment. Thus, sedimentation acts not only as a sink of fog liquid water but also as a mechanism connecting fog-top microphysical growth with the vertical structure and evolution of the fog layer.

The LWP budget quantitatively confirms the competing roles of radiative liquid-water production and sedimentation loss. In the NoDiurnal experiment, the radiation term is the dominant positive contribution, whereas fog-base sedimentation is the largest negative contribution. Thus, sedimentation offsets roughly two-thirds of the radiatively driven liquid-water production (Fig. 11). The sensible heat term provides a smaller positive contribution of about 4 g m^{-2} h^{-1}, while latent heat flux, turbulent transport near the fog base, fog-top entrainment, and large-scale subsidence act as additional LWP loss terms. These results indicate that the LWP evolution of advection fog is primarily controlled by a balance between fog-top radiative cooling and droplet sedimentation, with other dynamical and thermodynamic processes providing secondary adjustments. Sedimentation by droplets with radii larger than 10 μm accounts for the dominant contribution to the total sedimentation sink (Figs. 10f and 10g). Although bimodal fog droplet spectra have long been observed (Gultepe et al., 2009; Isaac et al., 2020; Wang et al., 2020), this study provides a process-based explanation of how relatively large droplets systematically influence the evolution of sea fog.

The sensitivity experiments further confirm the importance of droplet sedimentation for advection-fog evolution (Fig. 12). In the NoSedi experiment, removing gravitational sedimentation causes excessive liquid-water accumulation, with near-surface LWC frequently exceeding 0.5 g m^{-3}, and raises the fog/cloud top by approximately 270 m relative to NoDiurnal by 00:00 UTC on July 4. In NoCollCoal, the suppression of collision–coalescence reduces the sedimentation loss from approximately -20 to -16 g m^{-2} h^{-1}, nearly doubling the total LWP tendency and accelerating the upward development of the fog layer. The aerosol-sensitivity experiments show that lower aerosol loading favors fewer but larger droplets and thus stronger sedimentation, whereas higher aerosol loading

https://doi.org/10.5194/egusphere-2026-2980
Preprint. Discussion started: 13 July 2026

produces more numerous and smaller droplets that weaken gravitational settling. Together, these experiments demonstrate that sedimentation is a key microphysical control on liquid-water accumulation, vertical fog development, and the fog-to-stratus transition in marine advection fog.

Several limitations should be considered when interpreting these results. First, the conclusions are based on a single advection-fog event over the northwestern Pacific. The HighAero and LowAero experiments further demonstrate that sedimentation is strongly influenced by the background aerosol population through its effect on large-droplet formation. Consequently, the quantitative results reported here may depend on aerosol concentration, the supply of sea-salt aerosols, and the meteorological conditions of the particular event. Second, direct in situ observations of droplet sedimentation over the ocean were unavailable. Although ship-based and satellite observations were used to evaluate the simulated fog evolution and microphysical properties, these observations cannot directly constrain the vertical droplet sedimentation flux. Moreover, the present study focuses on gravitational sedimentation and does not explicitly assess near-surface turbulent droplet deposition, which previous studies have identified as an important liquid-water removal pathway (Katata et al., 2011; Taylor et al., 2021). This omission may affect estimates of the total liquid-water loss and its partitioning among removal processes near the fog base. These limitations largely reflect the scarcity of direct measurements over the open ocean. Nevertheless, the sensitivity experiments support the robustness of the qualitative mechanism identified here, although its quantitative magnitude remains case-dependent.

Within these constraints, the findings have two broader implications for understanding and modelling marine advection fog. First, the role of droplet sedimentation extends beyond near-surface liquid-water removal. Previous studies have suggested that droplet settling or deposition near the sea surface can reduce fog water content and alleviate the excessive-LWC bias in numerical simulations (Taylor et al., 2021). Our results extend this view by showing that sedimentation systematically influences the liquid-water budget and vertical evolution of the entire fog layer.

Specifically, in the NoDiurnal experiment, sedimentation signals originate near the fog top, propagate downward through the fog layer, and contribute to delayed liquid-water removal near the fog base. The NoSedi experiment further shows that removing sedimentation not only increases the liquid water content but also substantially elevates the top of the fog/cloud layer and alters its vertical development. These findings indicate that droplet sedimentation should be regarded not merely as a lower-boundary sink but as a vertically coupled microphysical process that regulates liquid-water redistribution, fog-top

https://doi.org/10.5194/egusphere-2026-2980
Preprint. Discussion started: 13 July 2026

radiative feedbacks, and fog-layer development. Together, these results refine the conceptual framework for advection-fog evolution illustrated in Fig. 1.

Another implication concerns aerosol depletion within the fog layer. Previous observations have reported a rapid decrease in aerosol number concentration before and during sea-fog events (Fernando et al., 2025; Zhao et al., 2022), often by one to two orders of magnitude. The present simulations reproduce a marked aerosol reduction after fog formation and suggest that droplet sedimentation contributes to this depletion by removing activated aerosol particles through condensational growth and gravitational settling (Fig. 7d). Therefore, sedimentation affects not only the liquid-water budget but also the aerosol budget of the fog layer. This implies that accurate sea-fog simulation requires a realistic representation of aerosol replenishment, especially sea-salt aerosol emissions from the ocean surface.

Code and data availability. UCLALES–SALSA is available from the official GitHub repository at https://github.com/UCLALES-SALSA/UCLALES-SALSA. The ICOADS observations used in this study are available from the NOAA National Centers for Environmental Information at https://www.ncei.noaa.gov/products/international-comprehensive-ocean-atmosphere-data-set. MODIS cloud products are available from NASA at https://modis.gsfc.nasa.gov/data/dataprod/mod06.php and through the LAADS DAAC data portal at https://ladsweb.modaps.eosdis.nasa.gov/. ERA5 reanalysis data are available from the Copernicus Climate Data Store at https://cds.climate.copernicus.eu/datasets/reanalysis-era5-single-levels. MERRA-2 aerosol data are available from the NASA Goddard Earth Sciences Data and Information Services Center at https://gmao.gsfc.nasa.gov/gmao-products/merra-2/data-access_merra-2/. The model outputs generated in this study are available from the corresponding author upon reasonable request because the complete model-output files are too large to be deposited in a public repository.

Author contributions. JWL conceptualized the study and designed the main scientific framework. SL performed the large-eddy simulations and model experiments. SL and WD analysed the data and prepared the initial draft of the manuscript. LY provided guidance on the use of the large-eddy simulation model. JWL revised and edited the manuscript. All authors discussed the results and contributed to reviewing and improving the manuscript.

https://doi.org/10.5194/egusphere-2026-2980
Preprint. Discussion started: 13 July 2026

Competing interests. The contact author has declared that none of the authors has any competing interests.

Financial support. This work is supported by the National Natural Science Foundation of China (U2342214 and 42275071). L. Y. is supported by the National Natural Science Foundation of China (42405085).

https://doi.org/10.5194/egusphere-2026-2980
Preprint. Discussion started: 13 July 2026

Reference

Barve, A., Gultepe, I., Joseph Fernando, H., Wang, Q., and Shen, L.: Large-eddy simulation with Lagrangian cloud modeling and large-scale dynamics (\ \mathrmL^3 \) for studying the marine fog life cycle, Quarterly Journal of the Royal Meteorological Society, 151, e5022, https://doi.org/10.1002/qj.5022, 2025.

Boutle, I., Price, J., Kudzotsa, I., Kokkola, H., and Romakkaniemi, S.: Aerosol–fog interaction and the transition to well-mixed radiation fog, Atmos. Chem. Phys., 18, 7827–7840, https://doi.org/10.5194/acp-18-7827-2018, 2018.

Calderón, S. M., Tonttila, J., Buchholz, A., Joutsensaari, J., Komppula, M., Leskinen, A., Hao, L., Moisseev, D., Pullinen, I., Tiitta, P., Xu, J., Virtanen, A., Kokkola, H., and Romakkaniemi, S.: Aerosol–stratocumulus interactions: towards a better process understanding using closures between observations and large eddy simulations, Atmos. Chem. Phys., 22, 12417–12441, https://doi.org/10.5194/acp-22-12417-2022, 2022.

Chen, C., Zhang, M., Perrie, W., Chang, R., Chen, X., Duplessis, P., and Wheeler, M.: Boundary Layer Parameterizations to Simulate Fog Over Atlantic Canada Waters, Earth and Space Science, 7, e2019EA000703, https://doi.org/10.1029/2019EA000703, 2020.

Fernandez, D., Kim, S., and Robinson, T.: Standard fog collector and dual FM-120 comparisons, Atmospheric Research, 315, 107869, https://doi.org/10.1016/j.atmosres.2024.107869, 2025.

Fernando, H. J. S., Dorman, C., Pardyjak, E., Shen, L., Wang, Q., Creegan, E., Gaberšek, S., Gultepe, I., Hoch, S., Lenain, L., Richter, D., Chang, R., VandenBoer, T. C., Bardoel, S., Barve, A., Blomquist, B., Bullock, T., Chen, Z., Colosi, L., Coppersmith, R. S., Crawford, I., Crilley, L. R., Dimitrova, R., Dowling, A., Eleuterio, D., Fiorino, S., Gallagher, M., Gapp, N., Giacosa, G., Grachev, A., Grare, L., Hintz, T., Hocut, C., Huang, K. Y., Hyde, O., Keefer, K., Ortiz-Suslow, D. G., Perelet, A., Perrie, W., Ruiz-Plancarte, J., Salehpoor, L., Singh, D., Statom, N., Taylor, P., Wang, S., and Yamaguchi, R.: Fatima-GB: Searching clarity within marine fog, Bulletin of the American Meteorological Society, https://doi.org/10.1175/BAMS-D-23-0050.1, 2025.

Gelaro, R., McCarty, W., Suárez, M. J., Todling, R., Molod, A., Takacs, L., Randles, C. A., Darmenov, A., Bosilovich, M. G., Reichle, R., Wargan, K., Coy, L., Cullather, R., Draper, C., Akella, S., Buchard, V., Conaty, A., Da Silva, A. M., Gu, W., Kim, G.-K., Koster, R., Lucchesi, R., Merkova, D., Nielsen, J. E., Partyka, G., Pawson, S.,

https://doi.org/10.5194/egusphere-2026-2980
Preprint. Discussion started: 13 July 2026

Putman, W., Rienecker, M., Schubert, S. D., Sienkiewicz, M., and Zhao, B.: The Modern-Era Retrospective Analysis for Research and Applications, Version 2 (MERRA-2), J. Climate, 30, 5419–5454, https://doi.org/10.1175/JCLI-D-16-0758.1, 2017.

Grainger, R. G.: Some Useful Formulae for Particle Size Distributions and Optical Properties, n.d.

Grosvenor, D. P., Sourdeval, O., Zuidema, P., Ackerman, A., Alexandrov, M. D., Bennartz, R., Boers, R., Cairns, B., Chiu, J. C., Christensen, M., Deneke, H., Diamond, M., Feingold, G., Fridlind, A., Hünerbein, A., Knist, C., Kollias, P., Marshak, A., McCoy, D., Merk, D., Painemal, D., Rausch, J., Rosenfeld, D., Russchenberg, H., Seifert, P., Sinclair, K., Stier, P., van Diedenhoven, B., Wendisch, M., Werner, F., Wood, R., Zhang, Z., and Quaas, J.: Remote Sensing of Droplet Number Concentration in Warm Clouds: A Review of the Current State of Knowledge and Perspectives, Reviews of Geophysics, 56, 409–453, https://doi.org/10.1029/2017RG000593, 2018.

Gryspeerdt, E., McCoy, D. T., Crosbie, E., Moore, R. H., Nott, G. J., Painemal, D., Small-Griswold, J., Sorooshian, A., and Ziemba, L.: The impact of sampling strategy on the cloud droplet number concentration estimated from satellite data, Atmos. Meas. Tech., 15, 3875–3892, https://doi.org/10.5194/amt-15-3875-2022, 2022.

Gultepe, I., Tardif, R., Michaelides, S. C., Cermak, J., Bott, A., Bendix, J., Müller, M. D., Pagowski, M., Hansen, B., Ellrod, G., Jacobs, W., Toth, G., and Cober, S. G.: Fog research: A review of past achievements and future perspectives, Pure appl. geophys., 164, 1121–1159, https://doi.org/10.1007/s00024-007-0211-x, 2007.

Gultepe, I., Pearson, G., Milbrandt, J. A., Hansen, B., Platnick, S., Taylor, P., Gordon, M., Oakley, J. P., and Cober, S. G.: The Fog Remote Sensing and Modeling Field Project, Bull. Amer. Meteor. Soc., 90, 341–360, https://doi.org/10.1175/2008BAMS2354.1, 2009.

Gultepe, I., Milbrandt, J. A., and Zhou, B.: Marine fog: A review on microphysics and visibility prediction, in: Marine Fog: Challenges and Advancements in Observations, Modeling, and Forecasting, edited by: Koračin, D. and Dorman, C. E., Springer International Publishing, Cham, 345–394, https://doi.org/10.1007/978-3-319-45229-6_7, 2017.

Hersbach, H., Bell, B., Berrisford, P., Hirahara, S., Horányi, A., Muñoz-Sabater, J., Nicolas, J., Peubey, C., Radu, R., Schepers, D., and others: The ERA5 global

https://doi.org/10.5194/egusphere-2026-2980
Preprint. Discussion started: 13 July 2026

reanalysis, Quarterly Journal of the Royal Meteorological Society, 146, 1999–2049, https://doi.org/10.1002/qj.3803, 2020.

Isaac, G. A., Bullock, T., Beale, J., and Beale, S.: Characterizing and Predicting Marine Fog Offshore Newfoundland and Labrador, Weather and Forecasting, 35, 347–365, https://doi.org/10.1175/WAF-D-19-0085.1, 2020.

Katata, G., Kajino, M., Hiraki, T., Aikawa, M., Kobayashi, T., and Nagai, H.: A method for simple and accurate estimation of fog deposition in a mountain forest using a meteorological model, Journal of Geophysical Research: Atmospheres, 116, https://doi.org/10.1029/2010JD015552, 2011.

Kokkola, H., Korhonen, H., Lehtinen, K. E. J., Makkonen, R., Asmi, A., Järvenoja, S., Anttila, T., Partanen, A.-I., Kulmala, M., Järvinen, H., Laaksonen, A., and Kerminen, V.-M.: SALSA – a Sectional Aerosol module for Large Scale Applications, Atmospheric Chemistry and Physics, 8, 2469–2483, https://doi.org/10.5194/acp-8-2469-2008, 2008.

Koračin, D., Dorman, C. E., Lewis, J. M., Hudson, J. G., Wilcox, E. M., and Torregrosa, A.: Marine fog: A review, Atmospheric Research, 143, 142–175, https://doi.org/10.1016/j.atmosres.2013.12.012, 2014.

Lilly, K. E.: The representation of small-scale turbulence in numerical simulation experiments, 1966.

Lin, Y.-L., Farley, R. D., and Orville, H. D.: Bulk parameterization of the snow field in a cloud model, Journal of Applied Meteorology and Climatology, 22, 1065–1092, https://doi.org/10.1175/1520-0450(1983)022%3C1065:BPOTSF%3E2.0.CO;2, 1983.

Mazoyer, M., Lac, C., Thouron, O., Bergot, T., Masson, V., and Musson-Genon, L.: Large eddy simulation of radiation fog: impact of dynamics on the fog life cycle, Atmos. Chem. Phys., 17, 13017–13035, https://doi.org/10.5194/acp-17-13017-2017, 2017.

Platnick, S., King, M. D., Ackerman, S. A., Menzel, W. P., Baum, B. A., Riedi, J. C., and Frey, R. A.: The MODIS cloud products: algorithms and examples from terra, IEEE Trans. Geosci. Remote Sensing, 41, 459–473, https://doi.org/10.1109/TGRS.2002.808301, 2003.

Seifert, A. and Beheng, K. D.: A double-moment parameterization for simulating autoconversion, accretion and selfcollection, Atmospheric Research, 59–60, 265–281, https://doi.org/10.1016/S0169-8095(01)00126-0, 2001.

https://doi.org/10.5194/egusphere-2026-2980
Preprint. Discussion started: 13 July 2026

Stevens, B., Moeng, C.-H., Ackerman, A. S., Bretherton, C. S., Chlond, A., De Roode, S., Edwards, J., Golaz, J.-C., Jiang, H., Khairoutdinov, M., Kirkpatrick, M. P., Lewellen, D. C., Lock, A., Müller, F., Stevens, D. E., Whelan, E., and Zhu, P.: Evaluation of Large-Eddy Simulations via Observations of Nocturnal Marine Stratocumulus, Monthly Weather Review, 133, 1443–1462, https://doi.org/10.1175/MWR2930.1, 2005.

Taylor, P. A., Chen, Z., Cheng, L., Afsharian, S., Weng, W., Isaac, G. A., Bullock, T. W., and Chen, Y.: Surface deposition of marine fog and its treatment in the Weather Research and Forecasting (WRF) model, Atmos. Chem. Phys., 21, 14687–14702, https://doi.org/10.5194/acp-21-14687-2021, 2021a.

Taylor, P. A., Chen, Z., Cheng, L., Afsharian, S., Weng, W., Isaac, G. A., Bullock, T. W., and Chen, Y.: Surface deposition of marine fog and its treatment in the Weather Research and Forecasting (WRF) model, Atmospheric Chemistry and Physics, 21, 14687–14702, https://doi.org/10.5194/acp-21-14687-2021, 2021b.

Tokinaga, H. and Xie, S.-P.: Ocean tidal cooling effect on summer sea fog over the Okhotsk Sea, Journal of Geophysical Research: Atmospheres, 114, https://doi.org/10.1029/2008JD011477, 2009.

Tonttila, J., Maalick, Z., Raatikainen, T., Kokkola, H., Kühn, T., and Romakkaniemi, S.: UCLALES–SALSA v1.0: A large-eddy model with interactive sectional microphysics for aerosol, clouds and precipitation, Geoscientific Model Development, 10, 169–188, https://doi.org/10.5194/gmd-10-169-2017, 2017.

Wang, S., Yi, L., Zhang, S., Shi, X., and Chen, X.: The Microphysical Properties of a Sea-Fog Event along the West Coast of the Yellow Sea in Spring, Atmosphere, 11, 413, https://doi.org/10.3390/atmos11040413, 2020.

Worley, S. J., Woodruff, S. D., Reynolds, R. W., Lubker, S. J., and Lott, N.: ICOADS release 2.1 data and products, International Journal of Climatology, 25, 823–842, https://doi.org/10.1002/joc.1166, 2005.

Xiang, Y., Zhang, Q., Wang, M., Kong, Y., and Huang, X.: A hybrid forecasting approach for sea fog based on machine learning, Artificial Intelligence for the Earth Systems, 5, 1–15, https://doi.org/10.1175/AIES-D-25-0013.1, 2025.

Yang, F., Sua, Y. M., Zheng, Z., Anderson, J., Sadi, H. F., Yeom, J. M., Singh, S. P., Hou, P., Cantrell, W. H., Lewis, E. R., Kostinski, A. B., and Shaw, R. A.: High-resolution lidar observations of sedimentation-induced size sorting of droplets near a laboratory cloud top, Proceedings of the National Academy of Sciences, 122, e2505421122, https://doi.org/10.1073/pnas.2505421122, 2025.

https://doi.org/10.5194/egusphere-2026-2980
Preprint. Discussion started: 13 July 2026

Yang, L., Liu, J.-W., Xie, S.-P., and Shen, S. S. P.: Transition from Fog to Stratus over the Northwest Pacific Ocean: Large-eddy Simulation, Monthly Weather Review, https://doi.org/10.1175/MWR-D-20-0420.1, 2021.

Yang, L., Ding, S., Liu, J.-W., and Zhang, S.-P.: Effects of radiative cooling on advection fog over the northwest Pacific Ocean: observations and large-eddy simulations, Atmos. Chem. Phys., 2024.

Yang, Y. and Gao, S.: The impact of turbulent diffusion driven by fog-top cooling on sea fog development, J. Geophys. Res. Atmos., 125, e2019JD031562, https://doi.org/10.1029/2019JD031562, 2020.

Yin, C., Shima, S., Xue, L., and Lu, C.: Simulation of marine stratocumulus using the super-droplet method: Numerical convergence and comparison to a double-moment bulk scheme using SCALE-SDM 5.2.6-2.3.1, Geoscientific Model Development, 17, 5167–5189, https://doi.org/10.5194/gmd-17-5167-2024, 2024.

Zhao, S., Yan, J., Lin, Q., Yao, L., Park, K., Jung, J., Chen, L., Xu, S., Sun, M., Wang, S., Yang, H., Shi, J., Zhang, M., and Sun, H.: Changes in aerosol particle composition during sea fog formation events in the sea ice regions of the Arctic Ocean, Atmospheric Environment, 272, 118943, https://doi.org/10.1016/j.atmosenv.2022.118943, 2022.

https://doi.org/10.5194/egusphere-2026-2980
Preprint. Discussion started: 13 July 2026

886 **Appendix A**

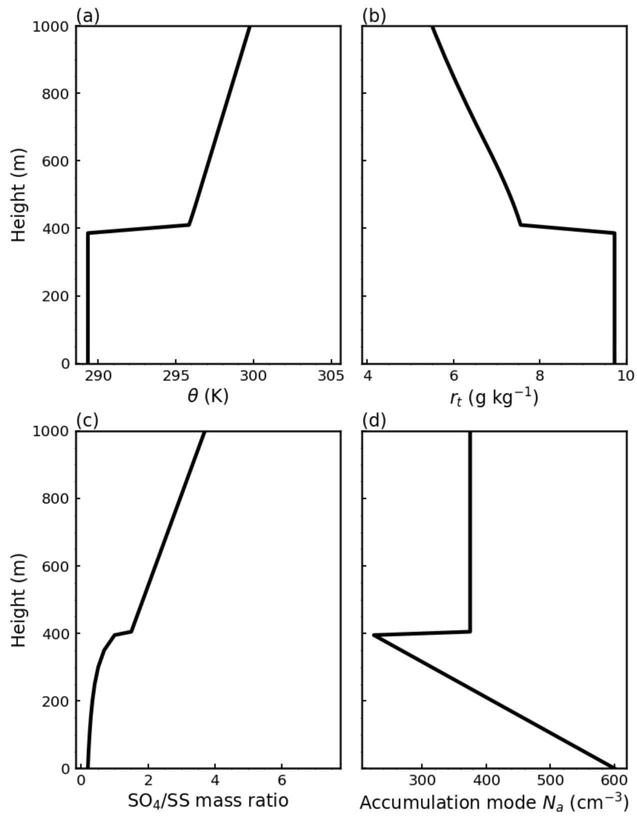

887

888 **Figure A1.** Vertical profiles used to initialize the simulation: (a) potential temperature (K), (b) total water
889 mixing ratio (g kg^{-}1), (c) sulfate to sea salt mass ratio and (b) accumulation-mode aerosol number
890 concentration (cm^{-3}).

https://doi.org/10.5194/egusphere-2026-2980
Preprint. Discussion started: 13 July 2026

Appendix B

This appendix provides the detailed formulations used to decompose the modelled LWP tendency into individual physical-process contributions following Wærsted et al. (2018). Tables B1 and B2 summarize the calculation methods for the LWP budget terms and the associated flux terms, respectively.

Table B1. LWP budget terms.

Physical process	Calculation methods
F_{rad}	$-\frac{s}{s+\gamma}\frac{1}{L_v}SH_{rad}$
F_{sedi}	$-F_{sedi,base}$
F_{SH}	$-\frac{s}{s+\gamma}\frac{1}{L_v}SH_{base}$
F_{LH}	$\frac{\gamma}{s+\gamma}\frac{1}{L_v}LH_{base}$
F_{turb}	$\rho_{a,base}\overline{w'q'_{liq\,base}}-\sum_j LWC_j\frac{\Delta h_j}{\Delta t}$
F_{ent}	$-\frac{s}{s+\gamma}\frac{1}{L_v}SH_{top}+\frac{\gamma}{s+\gamma}\frac{1}{L_v}LH_{top}+F_{liq\,top}$
F_{sub}	$-\frac{s}{s+\gamma}\frac{1}{L_v}SH_{sub}+\frac{d\,w_{ls}}{d\,z}LWP$

In Table B1, $s=de_s/dT$, $\gamma(L_v\,dq_v)/(c_p\cdot dt)=s\cdot dT_a/dt$, where q_v is the water vapor specific humidity, T_a is the fog-layer mean temperature, and w_{ls} is the large-scale vertical velocity. The subscript j denotes the corresponding physical quantity of the added layer. Table B2 presents the calculation methods for the flux terms listed in Table B1.

Table B2. Flux terms listed in Table B1.

Flux terms	Calculation methods
SH_{rad}	$F_{rad}^{\downarrow}-F_{rad}^{\uparrow}$
SH_{base}	$\rho_{a\,base}c_p\overline{w'\theta'_{base}}$
LH_{base}	$\rho_{a\,base}L_v\overline{w'q'_{v\,base}}$
SH_{top}	$-\rho_{a\,top}c_p\overline{w'\theta'_{top}}$
SH_{sub}	$\int_{CBH}^{CTH}\rho_a c_p\frac{g}{c_p}(-w_{ls})dz = \frac{1}{2}\rho_a g(-\frac{dw_{ls}}{dz})(CTH^2-CBH^2)$
LH_{top}	$-\rho_{a\,top}L_V\overline{w'q'_{v\,top}}-(-w_{ls,ab})\rho_{a,ab}L_V[q_s(T_{ab})-q_{v,ab}]-\sum_j\rho_{a,j}L_V[q_s(T_j)-q_{v,j}]\frac{\Delta h_j}{\Delta t}$
$F_{liq\,top}$	$-\rho_{a\,top}\overline{w'q'_{liq\,top}}+(-w_{ls,ab})LWC_{ab}+\sum_j LWC_j\frac{\Delta h_j}{\Delta t}+F_{sedi\,top}$

In Table B2, $F_{rad}^{\downarrow}$ and $F_{rad}^{\uparrow}$ represent the downward and upward radiative fluxes. The subscript "*base*" refers to the fog base layer, "*top*" refers to the fog top layer, and "*ab*" denotes the layer immediately above the fog top.